optica

Tunable quantum dot lasers grown directly on silicon

Yating Wan,[1,*,†] Sen Zhang,[2,†] Justin C. Norman,[3] M. J. Kennedy,[4] William He,[4] Songtao Liu,[4] Chao Xiang,[4] Chen Shang,[3] Jian-Jun He,[2] Arthur C. Gossard,[1,3,4] and John E. Bowers[1,3,4]

[1]Institute for Energy Efficiency, University of California Santa Barbara, Santa Barbara, California 93106, USA
[2]Centre for Integrated Optoelectronics, State Key Laboratory of Modern Optical Instrumentation, Zhejiang University, Hangzhou 310027, China
[3]Materials Department, University of California Santa Barbara, Santa Barbara, California 93106, USA
[4]Department of Electrical and Computer Engineering, University of California Santa Barbara, Santa Barbara, California 93106, USA
*Corresponding author: yatingwan@ucsb.edu

Received 19 July 2019; revised 26 September 2019; accepted 27 September 2019 (Doc. ID 373189); published 25 October 2019

Tunable semiconductor lasers are often listed in critical technology road maps for future dense-wavelength-division-multiplexing (DWDM) systems and high-performance computing systems, and they are increasingly demanded in long-haul, metropolitan, and access networks. The capability to produce such lasers directly on silicon (Si) could boost the use of Si photonics and facilitate the adoption of optical data transmission even at the chip scale. Moreover, just the use of Si as a cheap and large-diameter substrate for device production is very advantageous, as the fabrication can take advantage of the highly optimized processing techniques and economy of scale enabled by decades of development in Si microelectronics. Here, we report a tunable single-wavelength quantum dot (QD) laser directly grown on Si. The high carrier confinement and a real dot density of QDs provide reduced sensitivity to crystalline defects, which allows for exceptional lasing performance even in lattice-mismatched material systems. The discrete density of states of dots yields unique gain properties that show promise for improved device performance and new functionalities relative to the quantum well counterparts, including high temperature stability, low threshold operation, reduced sidewall recombination, and isolator-free stability. We implement a simple, integrable architecture to achieve over 45 dB side-mode-suppression-ratio without involving regrowth steps or subwavelength grating lithography. Under continuous-wave electrical injection at room temperature, we achieved a 16 nm tuning range with output powers of over 2.7 mW per tuning wavelength. This work represents a step towards using III–V/Si epitaxy to form efficient, easily manufacturable on-chip Si light sources for not only DWDM networks, but also spectroscopy, biosensors, and many other emerging applications.

https://doi.org/10.1364/OPTICA.6.001394

1. INTRODUCTION

Analogous to the historical scaling of CMOS technology, high-density photonic integrated circuits (PICs) allow optical systems previously restricted to bench-scale apparatuses to be developed in compact form factors with small footprint and low energy consumption [1]. Current PICs are based on either a III–V platform or a silicon (Si) platform with gain materials integrated via hybrid/heterogeneous integration [2]. Compared to the III–V platform, Si photonics greatly benefits from the mature fabrication processes in the microelectronics industry, the nearly defect-free substrates up to 450 mm in diameter, and the extremely high throughput processing lines at nanometer scale [3]. While hybrid integration requires precise alignment in the few micrometer or even submicrometer range that renders the whole process time-consuming and expensive, heterogeneous integration significantly relaxes the alignment tolerances as devices are defined lithographically after bonding the unpatterned III–V dies [4]. High overall efficiency has been achieved, with coupling losses lower than 0.5 dB/interface and backreflections better than −30 dB [5,6]. The whole PIC complexity has rapidly increased over the last decade, with over 400 components on a single waveguide, rivaling that of PICs on native substrates [7]. Commercial products are springing up, including Intel's 100G PSM4 QSFP transceivers and 100G CWDM4 transceivers. Meanwhile, this technology has been intensively investigated by a number of other companies, including Juniper Networks and HPE [8]. Nevertheless, relative to Si substrates, the III–V substrates required during the bonding process are orders of magnitude more expensive and are only available at much smaller wafer sizes that limit scalability [9,10].

Alternatively, monolithic integration via direct epitaxial growth is a straightforward wafer-level solution for low-cost and large-scale production if challenges of the heteroepitaxial growth can be properly managed [11]. While dislocation densities as low as 10^6 cm^{-2} have been reported, defect-free material or even material comparable to the state-of-the-art III–V wafers with defect level at 10^3 cm^{-2} remains elusive. This seriously degrades the reliability of conventional III–V devices on Si, particularly lasers,

where the most prolonged lifetime reported among GaAs-based quantum well (QW) lasers on Si is merely ~200 h after more than three decades of research [12]. On the contrary, in quantum dot (QD) devices, with typical dislocation densities of ~10^6–10^7 cm^{-2} in optimized III/V-on-Si buffers and typical dot densities of ~6×10^{10} cm^{-2}, the chance of charge carriers encountering a defect is far less than that of finding a dot and recombining radiatively. This leads to substantially longer device lifetimes [13]. Such an epitaxial approach with QDs as the active region not only provides a lower barrier to entry for Si photonics through the reduced sensitivity to defects [14–16], but also takes advantage of the many benefits inherent in QD devices, including high temperature stability [17–19], low threshold operation [20–22], reduced sidewall recombination [23–26], near zero linewidth enhancement factor [27], isolator-free stability at optical feedback levels of up to 90% [28], and most importantly, record-long device lifetimes on Si of more than 100 years at 35°C based on extrapolated 8000 h aging studies, and >100,000 h lifetimes at 60°C from extrapolated 4000 h aging studies [29].

While the emphasis for epitaxial III–V on Si research has thus far been on static performance of Fabry–Perot (FP)-type lasers, their performance has sufficiently improved to warrant investigation into more advanced laser configurations for more practical applications [30–32]. Recently, 4.1 Tb/s transmission using a single mode-locked laser grown on Si was demonstrated [33]. A distributed feedback (DFB) laser array grown on Si with a record wavelength range of 100 nm has been reported [34]. To further propel this technology to the marketplace, a tunable laser directly grown on Si is a critical milestone for optical communication systems to serve as backup transmitter sources and as components of wavelength routing devices. This type of laser could be set to any desired wavelength and thus eliminate the necessity to keep hundreds of specific wavelength DFBs. In addition to the reduced manufacturing costs from inventory reduction, tunable lasers are also natural complementary components in reconfigurable optical-add-drop multiplexers, and optical switches of various kinds, where a simple, integrable, widely tunable architecture is important for the combination of such wavelength converters with passive wavelength routers [35]. So far, the most successful tunable laser diodes include ring-based lasers [6], distributed Bragg reflector (DBR) lasers [36], DFB lasers [37] integrated on Si through wafer bonding, sampled-grating distributed Bragg reflector (SG-DBR) lasers [38], and superstructure grating (SSG) DBR lasers [39] through regrowth steps on native substrates.

In this paper, we report, to the best of our knowledge, the first tunable QD laser directly grown on an industrial-standard (001) Si substrate in a simple, integrable architecture without involving multiple epitaxial regrowth or low throughput, nonuniform gratings. By synchronously adjusting the injection currents applied to the two cascaded half-wave-coupled ring resonators, the tunable laser can be operated over a range of more than 16 nm without thermoelectric cooler (TEC) tuning. Eleven-channel and 37-channel wavelength switching is demonstrated, with a minimum side mode suppression ratio (SMSR) of 45 dB and 30 dB, respectively, producing output powers exceeding 2.7 mW per tuning wavelength under continuous-wave (CW) electrical injection.

2. DEVICE DESIGN

The tunable laser comprises two all-active ring resonators (R_1, R_2) coupled to a common FP cavity by two half-wave couplers, as shown in the schematic in Fig. 1(a) and the scanning electron microscopy (SEM) image in Fig. 1(b). The whole structure has been made from the same material and processed simultaneously. Therefore, the cross-sectional SEM images of the rings, couplers, and FP cavity are essentially the same, as shown in Fig. 1(c). The concept of the half-wave coupler was first proposed by He *et al.* [40], where the cross-coupling coefficients of the coupler have a π phase difference to the self-coupling coefficients. Contrary to conventional multimode-interference (MMI) with a $\pi/2$ phase difference and complementary power transfer functions in the two output waveguides, the half-wave coupler produces synchronous power transfer in the two output waveguides and can be engineered to achieve high SMSR when properly designing the coupling coefficients [40]. This structure has been popularized in an all-active two-section FP design [41–45] and a double rectangular ring-FP cavity embodiment [46], offering telecom suitable SMSR with a much simpler and more robust fabrication process compared to grating-based lasers. Here, two half-wave couplers were placed between each of the ring resonators and the common FP cavity, where the coupling coefficients $C_{11}, C_{12}, C_{21}, C_{22}$ represent the field amplitude coupling from common FP to itself, common FP to ring, ring to common FP, and ring to itself, respectively, as shown in Fig. 1(d). A zoomed-in view of the coupler and the distribution of the electrodes are shown in Fig. 1(e). The two ring resonators have slightly different cavity lengths with different wavelength periods, which are defined as the free spectral range (FSR),

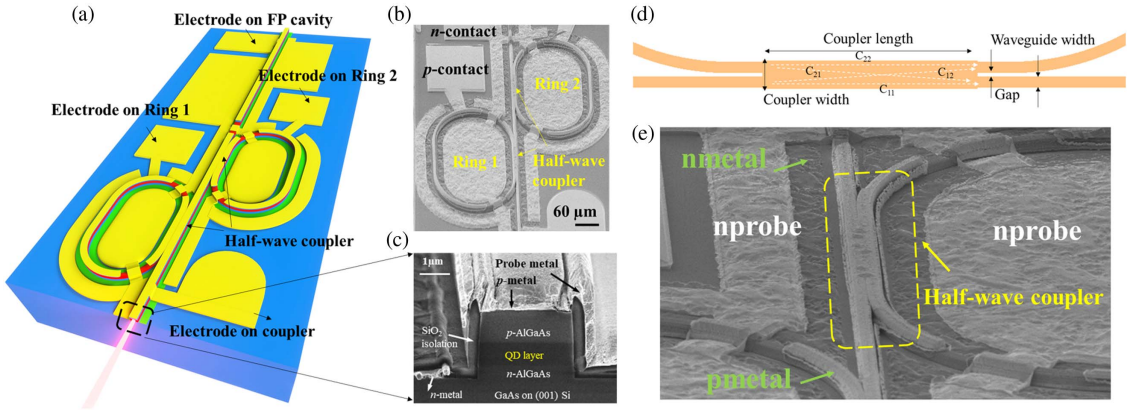

Fig. 1. (a) Schematic image and (b) top view SEM image of the tunable laser; (c) cross-sectional SEM of the laser architecture; (d) schematic image of the half-wave coupler with coupling element and various design parameters; (e) cross-sectional SEM of the half-wave coupler.

$$\mathrm{FSR}_{\mathrm{ring}} = \frac{c}{n_g L_r}, \tag{1}$$

where c is the speed of light, n_g is the effective group index, and L_r is the perimeter of the ring resonator. Therefore, the transmission function of the two comb sets have slightly different peak spacings, producing Vernier effects with an enlarged FSR of the combined cavity, defined as

$$\mathrm{FSR}_{\mathrm{cavity}} = \frac{\mathrm{FSR}_{R1} \cdot \mathrm{FSR}_{R2}}{\mathrm{FSR}_{R1} - \mathrm{FSR}_{R2}}, \tag{2}$$

and can effectively select one channel from the multiple lasing peaks of the FP cavity, as schematically illustrated in Fig. 2(a).

The length of the FP cavity is set to be 1050 μm, so that the longitudinal mode spacing of the laser is about 0.2 nm. The perimeter of R_1 is designed to be 583 μm, corresponding to an FSR_{R1} of 0.7 nm. When the path length difference of the other ring resonator decreases from 10% to 1%, the tuning range—as determined by the enlarged FSR of the combined cavity (FSR_c)—increases accordingly, as shown in Fig. 2(a). However, the tuning range cannot increase infinitely as it will, at the same time, compromise the SMSR, which is directly proportional to the threshold difference between the side mode and the main mode and inversely related to the cavity length difference [40]. The perimeter of R_2 is thus designed to be 563 μm, corresponding to a cavity difference of 3.4% and a tuning range of 21 nm. While this tuning mechanism using the Vernier effect is similar to the structure reported in [47], where two passive rings were coupled to a common FP cavity with a conventional MMI, the designed laser here does not require a second epitaxial regrowth or bandgap engineering for active-passive integration, and the transmission

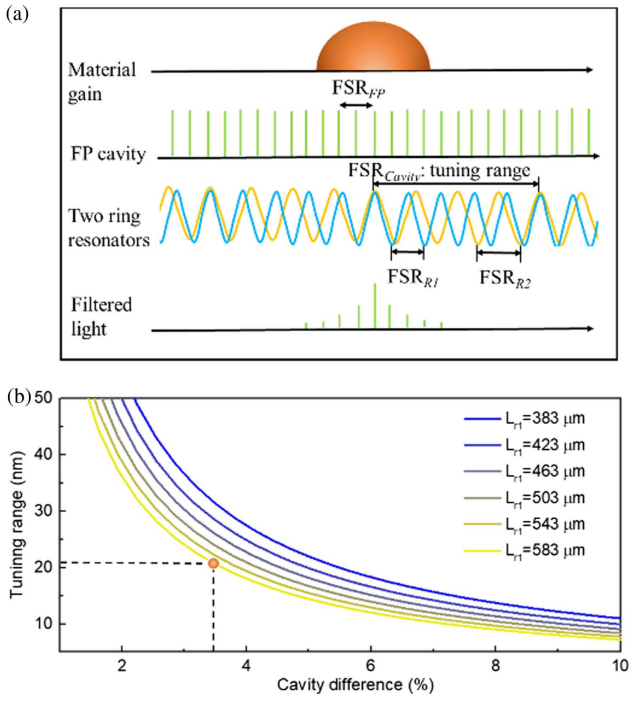

Fig. 2. (a) Schematic diagram illustrating the tuning principle of the tunable laser comprising two all-active ring resonators coupled to a common FP cavity; (b) calculated coupled cavity $\mathrm{FSR}_{\mathrm{cavity}}$ as a function of path length difference between the ring cavities for different values of the perimeter of R_1. The orange spot refers to the design point with a cavity difference of 3.4% and a tuning range of 21 nm.

phase is much less sensitive to the injection current variation by virtue of the half-wave couplers. This makes it possible to realize an optimal coupling coefficient in both amplitude and phase simultaneously with no or little theoretical loss, thereby achieving high SMSR by properly designing the coupler length and gap.

It has been demonstrated that the deviation of the cross-coupling phase from half-wave (i.e., 180°) will decrease the maximum threshold gain difference [40]. Furthermore, as the cross-coupling coefficient decreases, the mode selectivity between adjacent modes will improve as the peaks of the effective reflection factor become narrower [40]. Therefore, to maintain the optimum performance of the half-wave coupler, it is important that there is a range of low cross-coupling coefficients with a 180° phase difference between the two outputs of the coupler, where the normalized cross-coupling coefficient is defined as

$$\chi = \frac{|C_{21}|^2}{|C_{11}|^2 + |C_{21}|^2} = \frac{|C_{12}|^2}{|C_{12}|^2 + |C_{22}|^2}. \tag{3}$$

In Fig. 3, the amplitude and phase of the normalized cross-coupling coefficient is plotted as a function of the coupler length and the

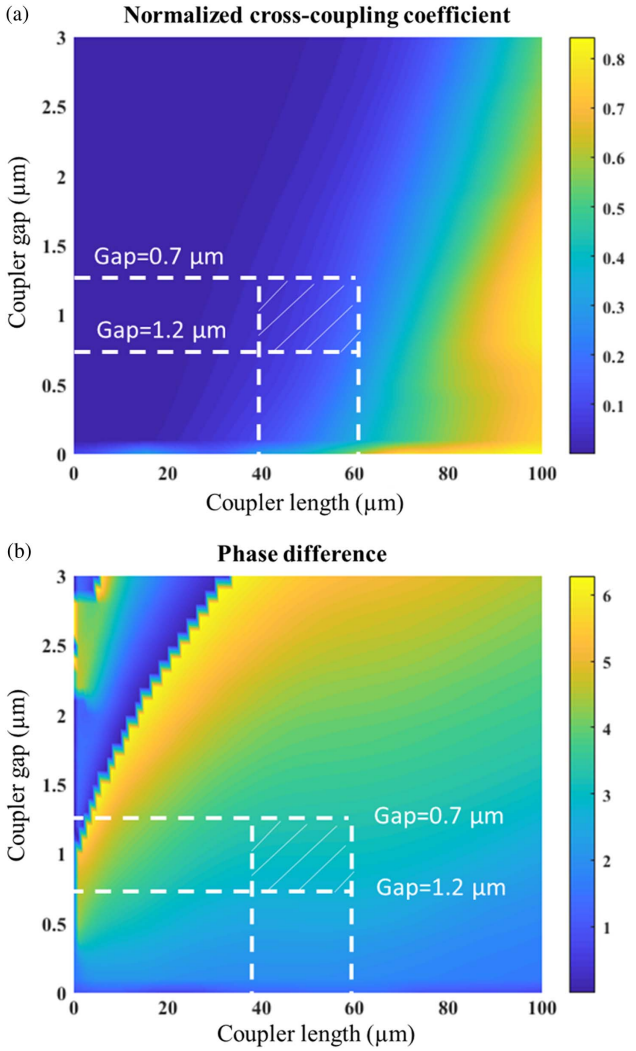

Fig. 3. (a) Amplitude and (b) phase of the normalized cross-coupling coefficient as a function of the coupler length and gap when $L_{r1} = 583$ μm, $L_{r2} = 563$ μm. The area with white dashes refers to the designed region.

coupler gap, respectively. The half-wave coupler was thus designed with a coupler length of 40–60 μm and a gap of 0.7–1.2 μm by further considering the fabrication-related constraints.

3. GROWTH AND FABRICATION

The tunable InAs/GaAs QD laser structure was directly grown on an on-axis (001) GaP/Si substrate by solid-source molecular beam epitaxy (MBE). The GaP/Si (001) on-axis wafer is commercially available in 300 mm size from $NASP_{III/V}$ GmbH. The inset in Fig. 4(a) shows the detailed QD epitaxial structure. A high crystalline quality GaAs buffer layer was first grown on Si with a low threading dislocation density of 7×10^6 cm^{-2} by optimizing the InGaAs/GaAs strained superlattice dislocation filter layers and a thermal cyclic annealing process [48].

The buffer was then followed by a 500 nm heavily *n*-type doped GaAs contact layer and a 1400 nm *n*-type AlGaAs cladding layer. The active region is composed of seven layers of InAs/InGaAs dots-in-a-well (DWELL) structures separated by 37.5 nm of unintentionally doped GaAs spacer layers. The thickness and growth temperature of the DWELL structure was varied to give different QD gain peak positions at different layers. This chirp design [49] gives rise to a photoluminescence (PL) spectrum with a broadened full width at half-maximum (FWHM) of 127 nm. Figure 4 shows the PL spectra from the as-grown QDs under increasing excitation power at room temperature. Only ground state emission was observed, with a peak centered around 1240 nm. The growth was completed with the deposition of a 1400 nm *p*-type AlGaAs cladding and a 300 nm heavily doped *p*-type GaAs contact layer.

The device fabrication began with a 500 nm thick plasma-enhanced-chemical-vapor-deposition SiO_2 layer, which defined the mesa region of the ring resonators, FP cavity, and the two half-wave couplers. The hard mask patterns were transferred to the heteroepitaxial wafer with a 3.8 μm deeply etched waveguide structure using inductively coupled plasma with a Cl_2/N_2-based chemistry. It is worth mentioning that in QW lasers, the carrier in-plane diffusion length reaches several micrometers and can readily reach the device sidewalls. Consequently, waveguides made of active material need to be shallowly etched, as radiative recombination efficiency drops drastically with the exposure of the active region. This complicates the process for QW-based half-wave-coupled rectangular ring FP lasers [46], since rectangular ring resonators instead of circular rings need to be used to avoid deep etching in the active waveguides. Furthermore, extra deeply etched total internal reflection mirrors are required to turn the direction of the light within the shallowly etched rectangular ring resonators, which greatly increases the cavity loss. However, since QDs are used as the active region here, the in-plane diffusion length is reduced to ~0.5 μm [50]. This enhanced carrier localization gives rise to much weaker surface recombination effects and enables a deeply etched process through the active layer for all the components of the device without imposing an obvious penalty on the lasing threshold. After the cavity etch, the fabrication process proceeded in a way similar to that of a standard ring/FP laser with the addition of an isolation etching step for separate control of the ring resonators, common FP cavity, and half-wave couplers. During the isolation etch, the heavily doped *p*-contact GaAs layer was etched away with ~600 nm depth into the *p*-type cladding layer, yielding a measured isolation resistance of around 15 kΩ between sections. Finally, the Si substrate was thinned to ~120 μm, and the laser facets were formed by cleaving with no facet coating applied to the surface.

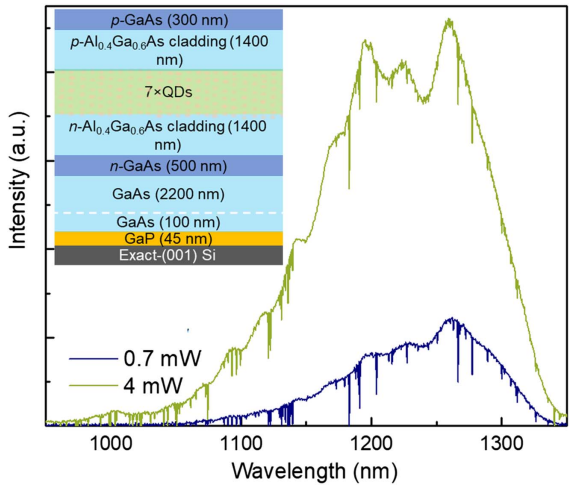

Fig. 4. High excitation (4 mW) and low excitation (0.7 mW) PL spectra of the as-grown QDs at room temperature. Inset, epitaxial layer structure of the tunable laser.

4. MEASUREMENT AND RESULTS

The tunable QD lasers are then measured by mounting onto a temperature-controlled copper plate at 20°C with a TEC. Figure 5(a) shows representative light–current–voltage (LIV) characteristics for a device with a coupler length of 60 μm and a coupler gap of 1.1 μm. The injection current on the half-wave coupler (I_c) was scanned while the injection currents on $R_1(I_{r1})$, $R_2(I_{r2})$, and FP cavity (I_{FP}) were fixed with three independent current sources at 60, 30, and 79 mA, respectively. A 1 V turn-on voltage and a 5.6 Ω differential series resistance from the I–V curve indicated good metal contacts for efficient current injection. A clear knee from the L-I curve is observed at the lasing threshold current of 33 mA. Maximum output power reached 2.7 mW per facet at an injection current of 3 times the threshold. We also measured standard FP lasers with the same epitaxial structure and the same etch depth. An FP cavity with a cavity length of 1050 μm and a cavity width of 3 μm shows a threshold current of 47 mA and a transparency current of 11 mA. The relatively large threshold current compared to our previous QD lasers [20] is due to the chirped QD design that decreases the differential gain. From Fig. 3, we can see that this half-wave coupler design

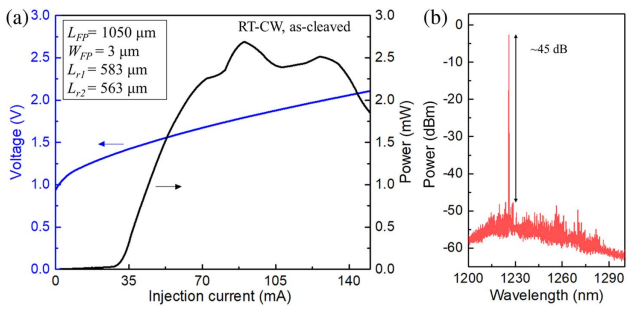

Fig. 5. (a) LIV curve by varying current on the half-wave coupler while keeping other sections constant; (b) single-mode lasing with SMSR ~45 dB.

corresponds to a π phase difference and a low cross-coupling coefficient of 0.16. This leads to single-wavelength emission with high SMSR of over 45 dB when $I_c = 67$ mA, $I_{\mathrm{FP}} = 79$ mA, $I_{r1} = 60$ mA, and $I_{r2} = 30$ mA, as shown in Fig. 5(b).

Wavelength tuning is accomplished by pumping the half-wave coupler and FP cavity region to transparency and tuning the current in either ring resonator. By changing the injection current on R_1 while keeping the other three electrodes biased at fixed current values as $I_c = 67$ mA, $I_{\mathrm{FP}} = 79$ mA, and $I_{r2} = 30$ mA, 11 lines with minimum SMSR of 45 dB and uniform line spacing of 0.75 nm can be obtained, as shown in Fig. 6.

The corresponding wavelength redshift of the main mode as a function of the tuning current of R_1 is presented in the inset in Fig. 6. By adjusting the injection currents on the two ring resonators synchronously while keeping the injection currents on the half-wave couplers and the FP cavity at 67 and 79 mA, respectively, 37-channel wavelength switching with a 16 nm tuning range and a minimum SMSR of 30 dB can be achieved, as shown in Fig. 7(a). Increasing the injection current in the tuning electrodes tends to increase the output power, but at the same time, increases the local temperature that lowers the quantum efficiency and reduces the output power. Therefore, SMSRs are about 45 dB for the main channels but are degraded to 30 dB for certain channels due to the counterbalance of the two effects and the material gain variations. The point plot in Fig. 7(b) summarizes the tuning information by directly plotting the wavelength of the main mode as a function of the injection current from R_1. When the injection current of R_1 is set at 34, 61, and 83 mA, mode-hopping by one FSR was observed. Within each FSR section, the wavelength increases with the increment of the injection current from R_1, indicating that the tuning is essentially dominated by the thermo-optic effect.

Currently, the tuning range is a bit smaller than the theoretical calculated FSR, as the refractive index variation is limited by the injection currents [51]. In the future, this can be increased by decreasing the perimeter difference of the two ring resonators. The tuning range can also be extended by varying the TEC temperature. For the GaAs-based material system, the gain spectrum redshifts at a rate of about 0.35 nm/°C with the increasing

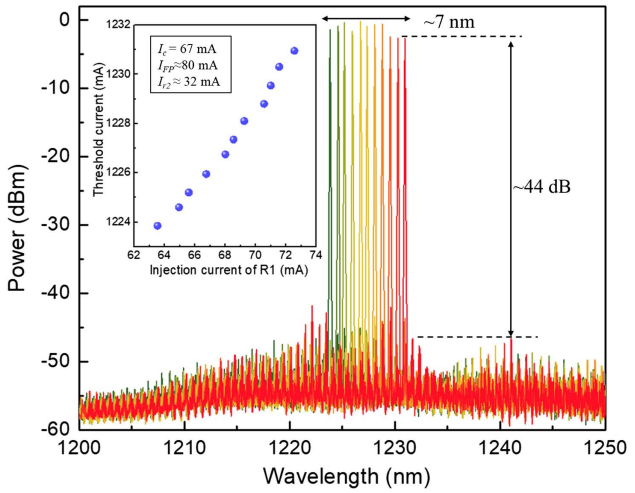

Fig. 6. Superimposed tuning spectra with 11-channel wavelength switching and a minimum SMSR of 45 dB. Inset, wavelength redshift of the main mode as a function of the tuning current of I_{r1}.

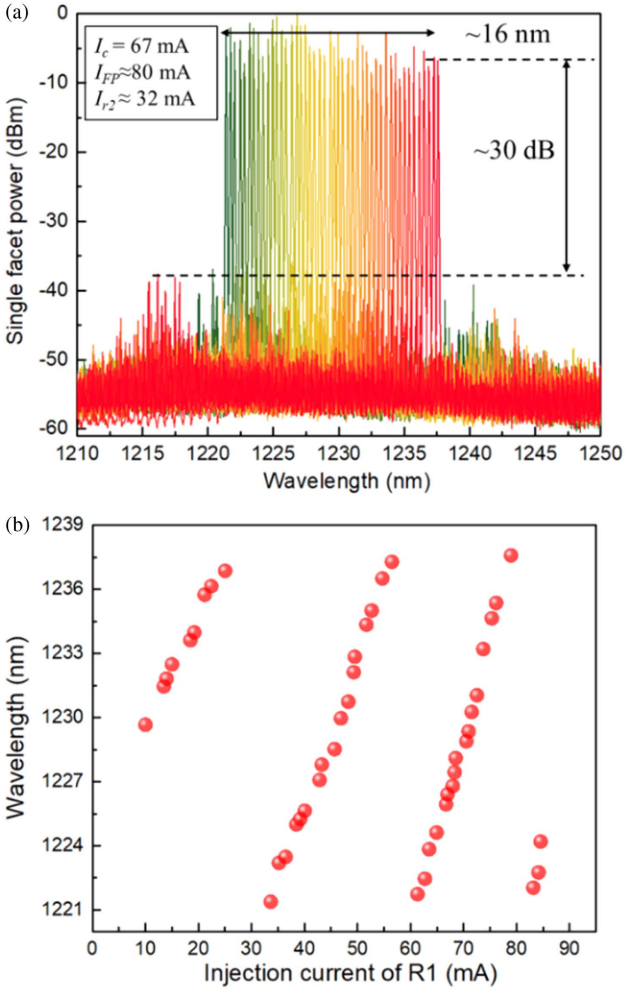

Fig. 7. Superimposed tuning spectra with 37-channel wavelength switching and minimum SMSR of 30 dB; (b) wavelength redshift of the main mode as a function of the tuning current of I_{r1}.

temperature. Therefore, the tuning range can be increased beyond the FSR determined by the perimeter difference of the ring resonators, to about 42 nm within a temperature range of 80°C. Furthermore, the chirped QD active region will be optimized to achieve a flat gain spectrum with maximum gain centered at 1.3 μm for O-band operation. Transmission experiments will be performed to investigate multiterabit/s optical interconnects for future large-scale Si electronic and PICs.

5. CONCLUSIONS

In conclusion, we demonstrated the first tunable QD single-wavelength laser directly grown on Si. Under CW electrical injection at room temperature, a 16 nm tuning range (without TEC tuning) was demonstrated with over 45 dB SMSR and output powers exceeding 2.7 mW per tuning wavelength. The capability of producing the tunable laser in a manufacturable single-step epitaxy process on Si indicates a potential road map towards future low-cost DWDM systems in integrated photonics applications.

Funding. National Natural Science Foundation of China (6196020600); Advanced Research Projects Agency-Energy (DE-AR0001042).

Acknowledgment. We are grateful to Dr. Lei Wang and the UCSB nanofabrication clean room staff for helpful discussions and assistance.

†These authors contributed equally to this work.

REFERENCES

1. M. Smit, J. van der Tol, and M. Hill, "Moore's law in photonics," Laser Photon. Rev. **6**, 1–13 (2012).
2. J. E. Bowers, D. Huang, D. Jung, J. C. Norman, M. A. Tran, Y. Wan, W. Xie, and Z. Zhang, "Realities and challenges of III-V/Si integration technologies," in *Optical Fiber Communication Conference* (2019), pp. Tu3E-1.
3. P. Dong, K. W. Kim, A. Melikyan, and Y. Baeyens, "Silicon photonics: a scaling technology for communications and interconnects," in *IEEE International Electron Devices Meeting (IEDM)* (2018), pp. 23.4.1–23.4.4.
4. O. Marshall, M. Hsu, Z. Wang, B. Kunert, C. Koos, and D. Van Thourhout, "Heterogeneous integration on silicon photonics," Proc. IEEE **106**, 2258–2269 (2018).
5. S. Dhoore, A. Köninger, R. Meyer, G. Roelkens, and G. Morthier, "Electronically tunable distributed feedback (DFB) laser on silicon," Laser Photon. Rev. **13**, 1800287 (2019).
6. D. Huang, M. A. Tran, J. Guo, J. Peters, T. Komljenovic, A. Malik, P. A. Morton, and J. E. Bowers, "High-power sub-kHz linewidth lasers fully integrated on silicon," Optica **6**, 745–752 (2019).
7. C. Zhang, S. Zhang, J. D. Peters, and J. E. Bowers, "$8 \times 8 \times 40$ Gbps fully integrated silicon photonic network on chip," Optica **3**, 785–786 (2016).
8. R. Jones, P. Doussiere, J. B. Driscoll, W. Lin, H. Yu, Y. Akulova, T. Komljenovic, and J. E. Bowers, "Heterogeneously integrated InP/silicon photonics: fabricating fully functional transceivers," IEEE Nanotechnol. Mag. **13**(2), 17–26 (2019).
9. Z. Zhou, B. Yin, and J. Michel, "On-chip light sources for silicon photonics," Light Sci. Appl. **4**, e358 (2015).
10. Z. Wang, A. Abbasi, U. Dave, A. De Groote, S. Kumari, B. Kunert, C. Merckling, M. Pantouvaki, Y. Shi, B. Tian, K. Van Gasse, J. Verbist, R. Wang, W. Xie, J. Zhang, Y. Zhu, J. Bauwelinck, X. Yin, Z. Hens, J. Van Campenhout, B. Kuyken, R. Baets, G. Morthier, D. Van Thourhout, and G. Roelkens, "Novel light source integration approaches for silicon photonics," Laser Photon. Rev. **11**, 1700063 (2017).
11. B. Kunert, Y. Mols, M. Baryshniskova, N. Waldron, A. Schulze, and R. Langer, "How to control defect formation in monolithic III/V hetero-epitaxy on (100) Si? a critical review on current approaches," Semicond. Sci. Technol. **33**, 93002 (2018).
12. Z. I. Kazi, P. Thilakan, T. Egawa, M. Umeno, and T. Jimbo, "Realization of GaAs/AlGaAs lasers on Si substrates using epitaxial lateral overgrowth by metalorganic chemical vapor deposition," Jpn. J. Appl. Phys. **40**, 4903–4906 (2001).
13. H. Liu, T. Wang, Q. Jiang, R. Hogg, F. Tutu, F. Pozzi, and A. Seeds, "Long-wavelength InAs/GaAs quantum-dot laser diode monolithically grown on Ge substrate," Nat. Photonics **5**, 416–419 (2011).
14. S. Chen, W. Li, J. Wu, Q. Jiang, M. Tang, S. Shutts, S. Elliott, A. Sobiesierski, A. Seeds, I. Ross, P. Smowton, and H. Liu, "Electrically pumped continuous wave III-V quantum dot lasers on silicon," Nat. Photonics **10**, 307–311 (2016).
15. Q. Feng, W. Wei, B. Zhang, H. Wang, J. Wang, H. Cong, T. Wang, and J. J. Zhang, "O-band and C/L-band IIIV quantum dot lasers monolithically grown on Ge and Si substrate," Appl. Sci. **9**, 385 (2019).
16. Y. Wan, Q. Li, A. Y. Liu, A. C. Gossard, J. E. Bowers, E. Hu, and K. M. Lau, "Optically pumped 1.3 μm room-temperature InAs quantum-dot micro-disk lasers directly grown on (001) silicon," Opt. Lett. **41**, 1664–1667 (2016).
17. T. Kageyama, K. Nishi, M. Yamaguchi, R. Mochida, Y. Maeda, K. Takemasa, Y. Tanaka, T. Yamamoto, M. Sugawara, and Y. Arakawa, "Extremely high temperature (220°C) continuous-wave operation of 1300-nm-range quantum dot lasers," in *Proceedings of the CLEO* (2011), paper PDA_1.
18. Y. Wan, Q. Li, A. Y. Liu, A. C. Gossard, J. E. Bowers, E. Hu, and K. M. Lau, "Temperature characteristics of epitaxially grown InAs quantum dot micro-disk lasers on silicon for on-chip light sources," Appl. Phys. Lett. **109**, 011104 (2016).
19. J. Kwoen, B. Jang, K. Watanabe, and Y. Arakawa, "High-temperature continuous-wave operation of directly grown InAs/GaAs quantum dot lasers on on-axis Si (001)," Opt. Express **27**, 2681–2688 (2019).
20. D. Jung, J. Norman, M. J. Kennedy, C. Shang, B. Shin, Y. Wan, A. C. Gossard, and J. E. Bowers, "High efficiency low threshold current 1.3 μm InAs quantum dot lasers on on-axis (001) GaP/Si," Appl. Phys. Lett. **111**, 122107 (2017).
21. Y. Wan, J. Norman, Q. Li, M. Kennedy, D. Liang, C. Zhang, D. Huang, Z. Zhang, A. Liu, A. Torres, D. Jung, A. Gossard, E. Hu, K. Lau, and J. Bowers, "1.3 μm submilliamp threshold quantum dot micro-lasers on Si," Optica **4**, 940–944 (2017).
22. T. Zhou, M. Tang, G. Xiang, X. Fang, X. Liu, B. Xiang, S. Hark, M. Martin, M. Touraton, T. Baron, Y. Lu, S. Chen, H. Liu, and Z. Zhang, "Ultra-low threshold InAs/GaAs quantum dot microdisk lasers on planar on-axis Si (001) substrates," Optica **6**, 430–435 (2019).
23. Y. Wan, Q. Li, A. Y. Liu, W. W. Chow, A. C. Gossard, J. E. Bowers, E. Hu, and K. M. Lau, "Sub-wavelength InAs quantum dot micro-disk lasers epitaxially grown on exact Si (001) substrates," Appl. Phys. Lett. **108**, 221101 (2016).
24. N. V. Kryzhanovskaya, A. E. Zhukov, M. V. Maximov, E. I. Moiseev, I. I. Shostak, A. M. Nadtochiy, Y. V. Kudashova, A. A. Lipovskii, M. M. Kulagina, and S. I. Troshkov, "Room temperature lasing in 1-μm microdisk quantum dot lasers," IEEE J. Sel. Top. Quantum Electron. **21**, 709–713 (2015).
25. Y. Wan, D. Jung, C. Shang, N. Collins, I. MacFarlane, J. Norman, M. Dumont, A. C. Gossard, and J. E. Bowers, "Low-threshold continuous-wave operation of electrically pumped 1.55 μm InAs quantum dash microring lasers," ACS Photon. **6**, 279–285 (2019).
26. Y. Wan, D. Inoue, D. Jung, J. C. Norman, C. Shang, A. C. Gossard, and J. E. Bowers, "Directly modulated quantum dot lasers on silicon with a milliampere threshold and high temperature stability," Photon. Res. **6**, 776–781 (2018).
27. Z. Zhang, D. Jung, J. Norman, W. W. Chow, and J. E. Bowers, "Linewidth enhancement factor in InAs/GaAs quantum dot lasers and its implication in isolator-free and narrow linewidth applications," IEEE J. Sel. Top. Quantum Electron. **25**, 1–9 (2019).
28. J. Duan, H. Huang, B. Dong, D. Jung, J. C. Norman, J. E. Bowers, and F. Grillot, "1.3-μm reflection insensitive InAs/GaAs quantum dot lasers directly grown on silicon," IEEE Photon. Technol. Lett. **31**, 345–348 (2019).
29. D. Jung, Z. Zhang, J. Norman, R. Herrick, M. J. Kennedy, P. Patel, K. Turnlund, C. Jan, Y. Wan, A. C. Gossard, and J. E. Bowers, "Highly reliable low-threshold InAs quantum dot lasers on on-axis (001) Si with 87% injection efficiency," ACS Photon. **5**, 1094–1100 (2017).
30. J. C. Norman, D. Jung, Y. Wan, and J. E. Bowers, "Perspective: the future of quantum dot photonic integrated circuits," APL Photon. **3**, 030901 (2018).
31. J. C. Norman, D. Jung, Z. Zhang, Y. Wan, S. Liu, C. Shang, R. W. Herrick, W. W. Chow, A. C. Gossard, and J. E. Bowers, "A review of high-performance quantum dot lasers on silicon," IEEE J. Quantum Electron. **55**, 1–11 (2019).
32. K. Li, M. Tang, M. Liao, J. Wu, S. Chen, A. Seeds, and H. Liu, "InAs GaAs quantum dot lasers monolithically integrated on group IV platform," in *IEEE International Electron Devices Meeting (IEDM)* (2018), pp. 23–25.
33. S. Liu, X. Wu, D. Jung, J. C. Norman, M. J. Kennedy, H. K. Tsang, A. C. Gossard, and J. E. Bowers, "High-channel-count 20 GHz passively mode-locked quantum dot laser directly grown on Si with 41 Tbit/s transmission capacity," Optica **6**, 128–134 (2019).
34. Y. Wang, S. Chen, Y. Yu, L. Zhou, L. Liu, C. Yang, M. Liao, M. Tang, Z. Liu, J. Wu, W. Li, I. Rose, A. J. Seeds, H. Liu, and S. Yu, "Monolithic quantum-dot distributed feedback laser array on silicon," Optica **5**, 528–533 (2018).
35. C. W. Coldren, G. A. Fish, J. S. Barton, L. Johansson, L. A. Coldren, and Y. Akulova, "Tunable semiconductor lasers: a tutorial," J. Lightwave Technol. **22**, 193–202 (2004).
36. T. Ferrotti, B. Blampey, C. Jany, H. Duprez, A. Chantre, F. Boeuf, C. Seassal, and B. B. Bakir, "Co-integrated 1.3 μm hybrid III-V/silicon tunable laser and silicon Mach-Zehnder modulator operating at 25 Gb/s," Opt. Express **24**, 30379–30401 (2016).
37. H. Duprez, A. Descos, T. Ferrotti, C. Sciancalepore, C. Jany, K. Hassan, C. Seassal, S. Menezo, and B. B. Bakir, "1310 nm hybrid InP/InGaAsP on silicon distributed feedback laser with high side-mode suppression ratio," Opt. Express **23**, 8489–8497 (2015).

38. V. Jayaraman, D. A. Cohen, and L. A. Coldren, "Demonstration of broadband tunability in a semiconductor laser using sampled gratings," Appl. Phys. Lett. **60**, 2321–2323 (1992).
39. H. Ishii, H. Tanobe, F. Kano, Y. Tohmori, Y. Kondo, and Y. Yoshikuni, "Quasicontinuous wavelength tuning in super-structure-grating (SSG) DBR lasers," IEEE J. Quantum Electron. **32**, 433–441 (1996).
40. J.-J. He and D. Liu, "Wavelength switchable semiconductor laser using half-wave V-coupled cavities," Opt. Express **16**, 3896–3911 (2008).
41. S. Zhang, J. Meng, S. Guo, L. Wang, and J.-J. He, "Simple and compact V-cavity semiconductor laser with 50×100 GHz wavelength tuning," Opt. Express, **21**, 13564–13571 (2013).
42. D. D'Agostino, D. Lenstra, H. P. M. M. Ambrosius, and M. K. Smit, "Coupled cavity laser based on anti-resonant imaging via multimode interference," Opt. Lett. **40**, 653–656 (2015).
43. J. Meng, X. Xiong, H. Xing, H. Jin, D. Zhong, L. Zou, J. Zhao, and J.-J. He, "Full C-band tunable V-cavity-laser based TOSA and SFP transceiver modules," IEEE Photon. Technol. Lett. **29**, 1035–1038 (2017).
44. S. Cheung, J. Matres, and M. R. Tan, "High-speed, directly-modulated widely tunable 1310 nm coupled cavity laser via multimode interference," J. Lightwave Technol. **37**, 2133–2139 (2019).
45. Y. Chu, Q. Chen, Z. Fan, and J.-J. He, "Tunable V-cavity lasers integrated with a cyclic echelle grating for distributed routing networks," IEEE Photon. Technol. Lett. **31**, 943–946 (2019).
46. L. Wu, X. Liao, Z. Hu, and J.-J. He, "Double half-wave-coupled rectangular ring-FP laser with 35 × 100 GHz wavelength tuning," IEEE Photon. Technol. Lett. **27**, 1076–1079 (2015).
47. S. Matsuo and T. Segawa, "Microring-resonator-based widely tunable lasers," IEEE J. Sel. Top. Quantum Electron. **15**, 545–554 (2009).
48. Y. Wan, D. Jung, J. Norman, C. Shang, I. MacFarlane, Q. Li, M. J. Kennedy, A. C. Gossard, K. M. Lau, and J. E. Bowers, "O-band electrically injected quantum dot micro-ring lasers on on-axis (001) GaP/Si and V-groove Si," Opt. Express **25**, 26853–26860 (2017).
49. M. Z. M. Khan, T. K. Ng, C.-S. Lee, P. Bhattacharya, and B. S. Ooi, "Chirped InAs/InP quantum-dash laser with enhanced broad spectrum of stimulated emission," Appl. Phys. Lett. **102**, 091102 (2013).
50. S. A. Moore, L. O'Faolain, M. A. Cataluna, M. B. Flynn, M. V. Kotlyar, and T. F. Krauss, "Reduced surface sidewall recombination and diffusion in quantum-dot lasers," IEEE Photon. Technol. Lett. **18**, 1861–1863 (2006).
51. W. Wei, H. Deng, and J.-J. He, "GaAs/AlGaAs-based 870-nm-band widely tunable edge-emitting V-cavity laser," IEEE Photon. J. **5**, 1501607 (2013).